

pubs.acs.org/cm Article

Tunable Growth of Layered Double Hydroxide Nanosheets through Hydrothermal Conversion of Atomic Layer Deposition Seed Layers

Published as part of Chemistry of Materials special issue "Precision Patterning".

Alondra M. Ortiz-Ortiz, Daniel O. Delgado Cornejo, Kalyn M. Fuelling, Ashley R. Bielinski, Tao Ma, and Neil P. Dasgupta*



Cite This: Chem. Mater. 2024, 36, 8300-8310



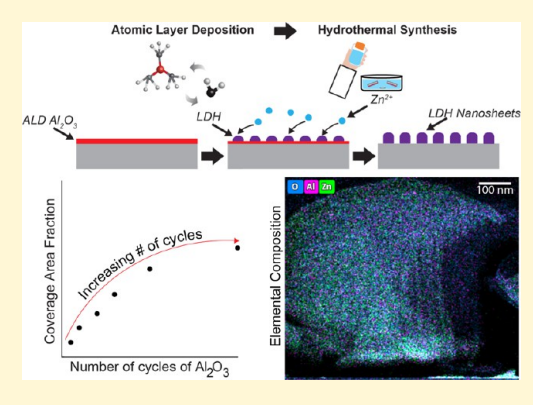
ACCESS

III Metrics & More

Article Recommendations

s Supporting Information

ABSTRACT: To enable the design and manufacturing of hierarchical nanomaterial architectures, there is a need for synthesis and processing methods that can enable tunable geometric control at the nanoscale while maintaining conformality on complex 3-D templates. In this study, we explore the programmable control of vertically oriented Zn–Al layered double hydroxide (LDH) nanosheet arrays using atomic layer deposition (ALD) to deposit a seed layer of Al₂O₃, which is subsequently consumed and converted into the LDH phase under hydrothermal growth conditions. We demonstrate tunable control over the spacing and length of the nanosheets by varying the thickness of the initial ALD seed layer with subnanometer precision. This can be viewed as a nanoscale titration reaction, where Al acts as the limiting reagent during the hydrothermal synthesis of the nanosheets. Elemental mapping demonstrates the dynamic evolution of the resulting morphology, which is driven by surface



diffusion and nucleation processes. The conformal nature of ALD allows for hierarchical growth of nanosheets on the surface of a variety of nonplanar substrate geometries, including microposts, paper fibers, and porous ceramic supports. This illustrates the power of ALD to enable bottom-up growth of 3-D nanoarchitectures with tunable geometries by controlling nucleation and growth in subsequent solution reactions.

■ INTRODUCTION

The synthesis of nanomaterials with tunable control of their geometry in three dimensions has attracted attention in recent years in applications such as semiconductors, catalysts, and batteries. A variety of bottom-up and top-down techniques have been developed with the aim of fabricating 2-D and 3-D nanostructures with control over their geometric parameters (e.g., feature size, shape, and orientation), which in turn affect the functional properties of the resulting material systems. This has led to the concept of "architected" materials, 12–14 where the process of conceptualizing, designing, and manufacturing nanostructured materials can approach the degree of control that can be achieved in macroscopic buildings and machines.

The ability to control and tune the geometric properties in nanoarchitected materials has been shown to enable advances in applications ranging from energy conversion/storage, biological interfaces, and structural materials. For example, vertically oriented nanowire (NW) arrays have been shown to facilitate tunable transport of electrons by controlling their separation and periodicity. In addition, ZnO NW arrays have been used to produce optoelectronic devices with tunable properties through control of their orientation and density. In

In electrochemical devices such as batteries and catalysts, the ability to tune electrode architectures results in the ability to decouple contributions of kinetics and mass transport. ^{17,18} For example, by tuning the length, spacing, and shell thickness of core—shell nanowire arrays, the photoelectrochemical performance of photoanode materials can be precisely optimized. ¹⁹ In the field of biology, the attachment and interactions of microorganisms of different sizes can be prevented or delayed by tuning the geometric properties of nanoarchitected surfaces. ²⁰ These examples help to highlight the importance of rationally tuning the geometrical properties of hierarchical nanomaterial systems to ensure precise control of the resulting functionality.

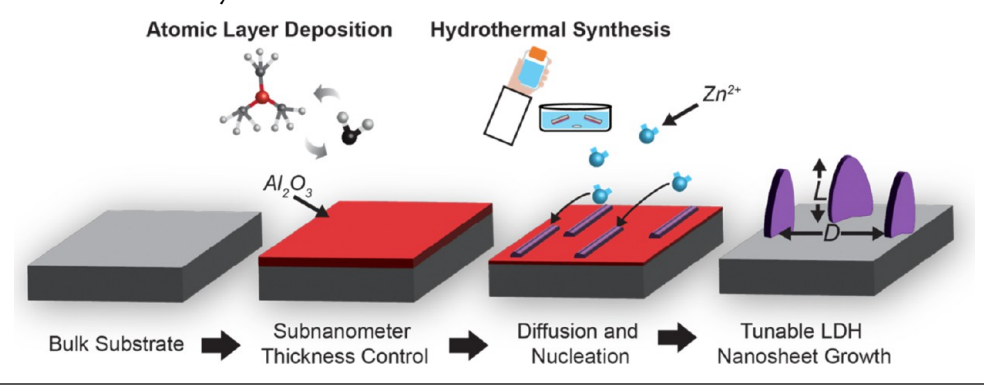
To enable rational control and patterning of nanoarchitected materials in three dimensions, a variety of bottom-up and top-down fabrication approaches have been developed. $^{21-23}$ Top-

Received: April 24, 2024 Revised: August 12, 2024 Accepted: August 13, 2024 Published: August 23, 2024





Scheme 1. Surface-Directed Assembly of LDH Nanosheets



down approaches include chemical etching, focused-ion beam milling, and laser ablation. ^{24–27} On the other hand, bottom-up approaches such as directed self-assembly, seeded hydrothermal/solvothermal synthesis, and additive manufacturing have also been of great interest in recent years. ^{28–30} Using these well-established processes, high resolution and control of geometric features can be achieved.

A common feature in many of these techniques is the requirement for a prepatterning step (e.g., photolithography, self-assembly), which can be increasingly difficult to implement when the geometric complexity of the substrates grows in three dimensions. This can result in challenges and trade-offs between reproducibility, geometric tunability, and conformal coverage, especially when attempting to pattern a nonplanar surface topology, which may include high-aspect-ratio features and/or re-entrant geometries that are not compatible with lineof-sight methods.³¹ Patterning and self-assembly processes can become particularly challenging when designing hierarchical material architectures such as hyperbranched geometries, which may be composed of multiple layers of dissimilar materials and geometries. Moreover, many patterning techniques suffer from low throughput and high costs, require high-temperature or high-vacuum processing, and are often limited to planar structures, which restricts their ability to control the resulting 3-D geometry over complex surfaces and large areas. Therefore, there is a continual need for new fabrication methods that can enable rational control of material geometry and composition at the nanoscale while facilitating integration into hierarchical 3-D substrate geometries.

A class of synthesis methods that has the potential to overcome some of these challenges can be categorized as "surface-directed assembly". 32 The surface-directed assembly approach is typically composed of a two-step process. First, a surface modification layer is deposited onto the underlying substrate, which can be in the form of a continuous film or discrete particles. A key requirement of this initial deposition step is that it must be highly conformal (to fully cover the underlying substrate geometry) while also being highly tunable (to control the surface properties that guide the following step). In the second step, the "information" that is encoded into the initial surface layer (i.e., control of surface composition, surface energy, surface morphology, grain size, etc.) is used to guide the subsequent growth of a 3-D nanostructured material (i.e., nanowires, nanoparticles, nanosheets, etc.) by exposing the surface to a reactive fluid, such as a gas or liquid. $^{33-35}$ Because the resulting material geometry is determined by the properties of the initial surface modification layer, this process can eliminate the need for lithography or

other patterning methods, enabling the programmable growth of hierarchical geometries on a diverse range of substrates.

As a model system, we have previously demonstrated a set of surface-directed assembly processes where atomic layer deposition (ALD) is used to deposit a seed layer of a given material (e.g., metal oxide), which can be used to guide the hydrothermal synthesis of ZnO nanowires (NWs) with tunable control of NW length, diameter, spacing, and angular orientation with respect to the substrate. 32,36 ALD was chosen because of its unique ability to combine subnanometer precision in the thickness and composition of the seed layer, while maintaining unparalleled conformality and uniformity of these properties on high-aspect-ratio surfaces. 37,38 Furthermore, since ALD is a low-temperature, low-vacuum process, it enables compatibility with a versatile range of substrates, including micro/nanopillars, fibers, porous and flexible polymers, and even biological substrates. Because it is not a line-of-sight technique, ALD can coat both convex and concave surface topologies, including those with re-entrant texture that would not be uniformly coated by using traditional physical vapor deposition (PVD) or solution-based methods. We have further demonstrated that the surface-directed assembly process can be scaled up to macroscopic objects with nonplanar surface geometries, which was facilitated by the development of a hydrothermal flow reactor.³⁵

To date, these previous demonstrations that used ALD for surface-directed assembly were based on the epitaxial growth of the NWs from the polycrystalline ALD seed layer, which remains intact during the hydrothermal growth process. ^{20,32,33,36,39} These epitaxial relationships can be further tuned by controlling the mechanical strain in the seed layer or by partially blocking nucleation sites with a secondary submonolayer overcoat using ALD. ³⁶

To build upon this platform, in this study, we explore an alternative approach for surface-directed assembly based on the conversion chemistry of the ALD seed layer during the hydrothermal synthesis process, which results in the formation of a secondary material phase on the surface. This builds upon prior demonstrations of solution-phase conversion chemistry of ALD films, including cation/anion exchange reactions, ^{40,41} formation of "grass-like" Al₂O₃, ^{42,43} hierarchical LDH nanotubes, ⁴⁴ 3D tubular hierarchical fibers, ⁴⁵ and metal—organic frameworks (MOFs). ⁴⁶ Additionally, there have been several examples of gas-phase conversion reactions of ALD films for anion/cation exchange or formation of new phases. ^{47–51}

However, to date, there is a lack of research into the use of ALD seed layers in conversion reactions to tune the 3-D geometric properties (e.g., feature size, shape, orientation) of

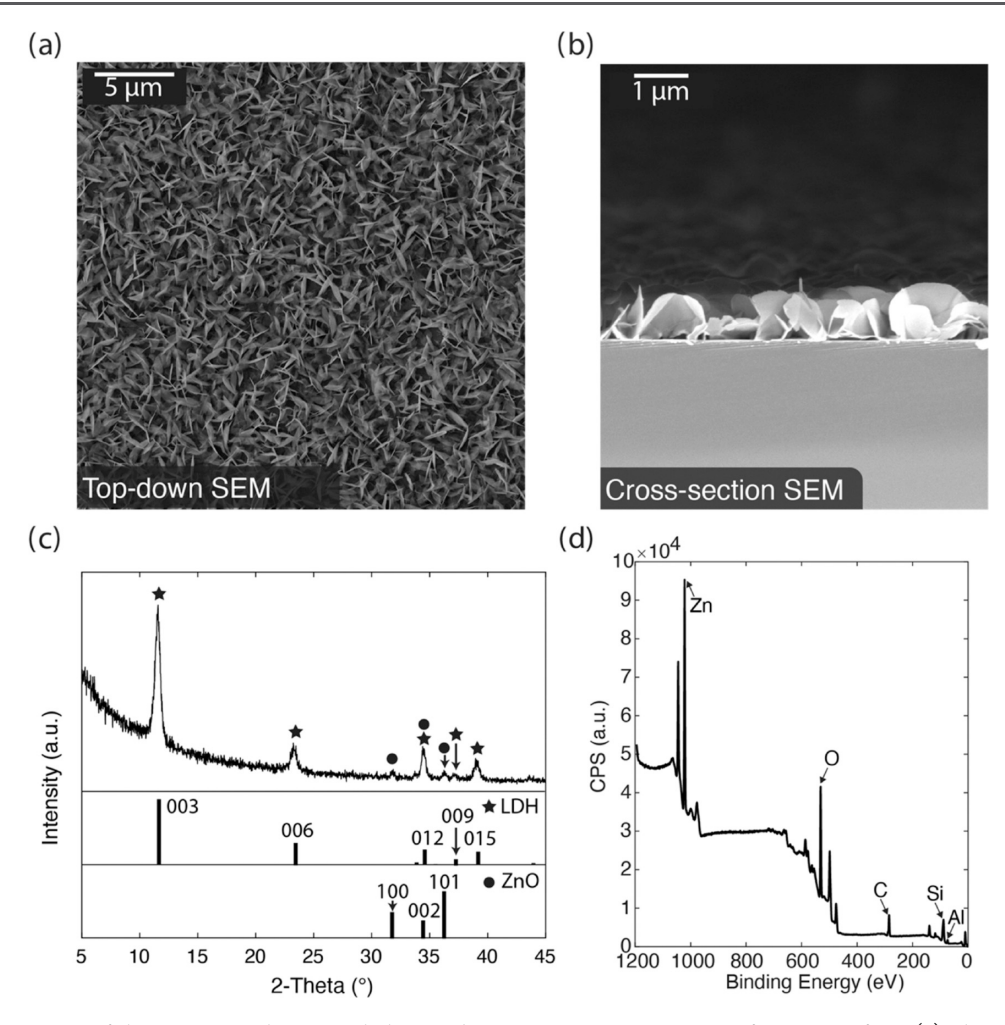


Figure 1. Characterization of the LDH nanosheet morphology and composition. SEM imaging of NS arrays from (a) plan-view and (b) cross-sectional perspective. (c) Grazing incidence XRD spectrum (LDH LPF Collection Code #1818345 and ZnO ICSD Collection Code #169463)^{61,62} and (d) XPS survey scan of the nanosheets.

the resulting new phase, which represents a complementary approach to the seeded hydrothermal synthesis methods described earlier. This would open up a new "toolbox" for material engineers to use the favorable properties of ALD described above, for the generation of a versatile range of nanoarchitected materials.

In this study, we introduce a new platform for surfacedirected assembly: first applying an Al₂O₃ seed layer of welldefined film thickness via ALD and then enabling its conversion to an array of Zn-Al layered double hydroxide (LDH) nanosheets (NSs) through a hydrothermal synthesis process, as shown in Scheme 1. By varying the number of ALD cycles (and thus changing the seed layer thickness with subnanometer resolution), we achieve tunable control of the inter-NS spacing and NS length. This ability to tunably control the resulting NS geometry is attributed to a sequence of surface diffusion, nucleation, and growth processes. These surface processes are quantitatively probed using scanning electron microscopy (SEM), X-ray diffraction (XRD), X-ray photoelectron spectroscopy (XPS), scanning transmission electron microscopy (STEM), and elemental mapping with energy-dispersive spectroscopy (EDS). Finally, we highlight the versatility of the ALD process by demonstrating that this programmable geometric control is retained when NSs are deposited on a variety of nonplanar surface geometries,

resulting in the formation of hierarchical nanomaterial architectures with potential applications in fields such as microplastics, electrocatalysis, and batteries. This new approach of surface-directed assembly based on the conversion of ALD films expands the ability of materials engineers to rationally control 3-D nanostructured geometries without the need for any lithographic patterning steps.

■ RESULTS AND DISCUSSION

Nanosheet Composition and Morphology. Figure 1a,b shows top-down and cross-sectional SEM images of the morphology of the synthesized Zn-Al LDH nanosheets. The nanosheet geometry is typical of the 2-D layered structure of the LDH material, which results in anisotropic growth in the in-plane vs through plane directions. 59,60 XRD analysis was performed to confirm the presence of the layered double hydroxide phase (Figure 1c), wherein the phase of the nanosheets is consistent with an LDH with a Zn:Al ratio of approximately 2:1.61 We note the presence of a minor ZnO impurity phase in the XRD spectra, which is a result of homogeneous precipitation of ZnO nanostructures in the hydrothermal growth solution that subsequently settle on the substrate surface. This phenomenon has been previously observed in surface-directed assembly of ZnO nanowires (refer to Figures S1 and S2) and does not affect the

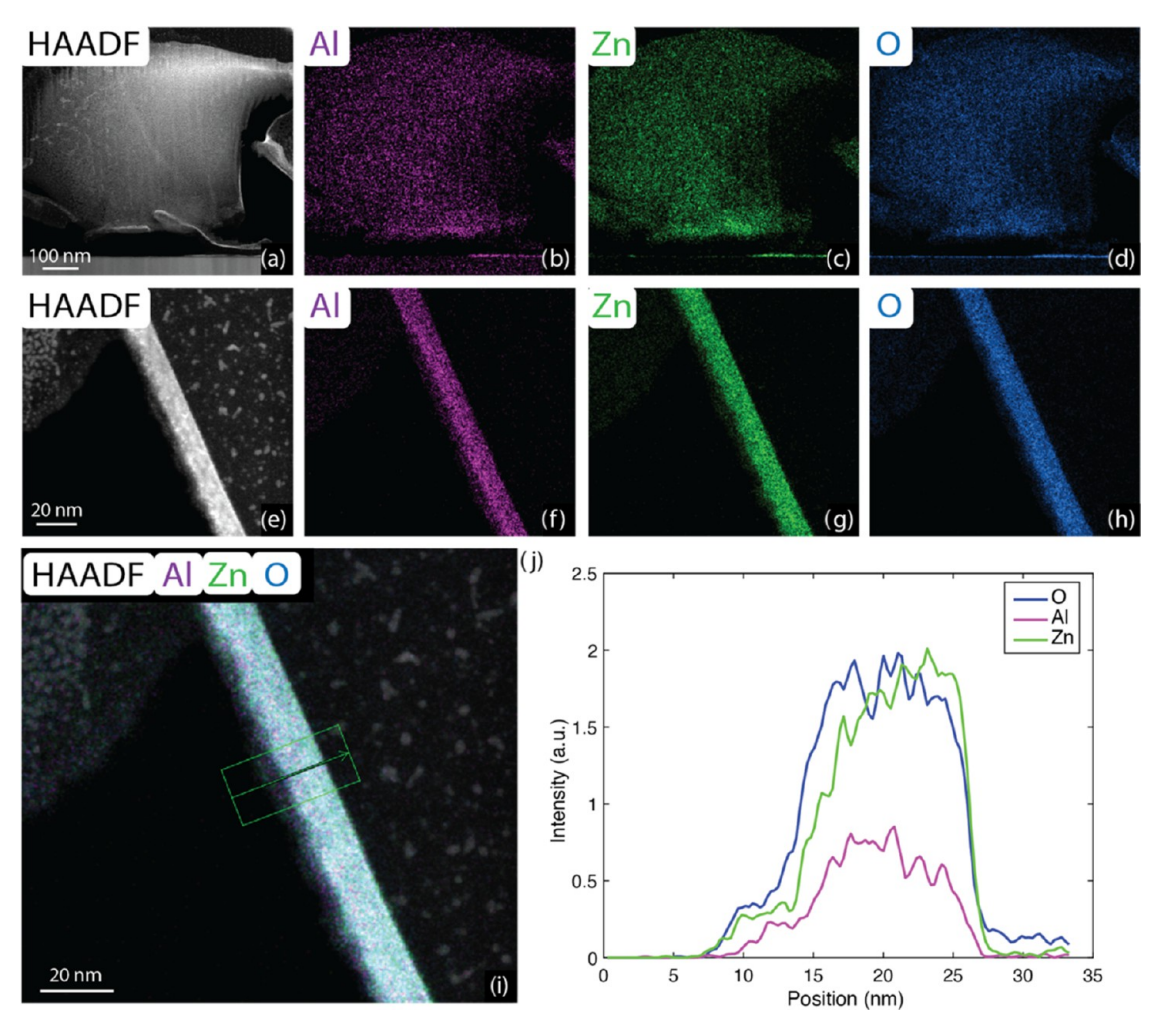


Figure 2. (a) Cross-sectional HAADF STEM image of a single nanosheet. EDS elemental mapping of (b) aluminum, (c) zinc, and (d) oxygen of the same nanosheet. (e) HAADF STEM image along the thickness direction of a single nanosheet. Elemental mapping showing distribution of (f) aluminum, (g) zinc, and (h) oxygen along the nanosheet thickness. (i) Composite EDS elemental map along the thickness, with (j) corresponding line scan. The green box denotes the location of the line scan.

heterogeneous growth of nanosheets on the substrate surface, which are observed in the SEM analysis to be the majority phase (Figure 1a,b). XPS analysis further confirms the surface composition to be Zn, Al, and O, with a Zn:Al ratio of approximately 2:1 (Figure 1d).

Figure 2 shows a high-angle annular dark-field (HAADF) STEM image of a single nanosheet. Energy-dispersive spectroscopy (EDS) analysis of the nanosheet was performed to study if any compositional gradients were present within a nanosheet. The Zn, Al, and O elemental profiles shown in Figure 2b—d,f—h show a uniform distribution of each element viewed along both the basal and edge planes. This is further confirmed by a line scan (Figure 2i,j) taken along the thickness of the nanosheet. The EDS analysis additionally confirms the Zn:Al ratio of approximately 2:1.

Tunable Control of Nanosheet Spacing. In our previous work on surface-directed assembly using nanocrystal-line ZnO seed layers, we demonstrated the ability to tune the geometric parameters of the resulting ZnO nanowire array (angular orientation, NW diameter, inter-NW spacing) by varying the number of ALD cycles. This was attributed to the epitaxial growth relationships between the seed layer and the resulting nanowires. However, for the formation of LDH NSs in this study, the ALD film serves as a coreactant during

the hydrothermal synthesis process, which is consumed during the reaction. We therefore hypothesize that the geometric properties of the resulting nanosheets may be tunable by varying the ALD film thickness, where the total number of Al atoms serves as the limiting reagent for the conversion reaction, which will influence the nucleation and growth processes.

To study the effect of the ALD seed layer thickness on the morphology of the resulting NS array, identical hydrothermal synthesis conditions (solution molarity, temperature, and reaction time) were used after different numbers of cycles of Al_2O_3 were deposited onto the substrate surface (Figure 3a–f). The thickness of the ALD seed layer increases linearly with the number of cycles of Al_2O_3 , as measured with ellipsometry (Figure S3). Figure 3a–f shows plan-view SEM images of the resulting NS arrays, where the spacing between nanosheets can be observed to monotonically decrease as a function of the Al_2O_3 film thickness (number of ALD cycles).

Image analysis was performed to quantify the areal surface coverage of the NS arrays as a function of the thickness of the initial ALD film (Figure 4). The increase in surface coverage is approximately linear until 30 cycles of Al₂O₃ are deposited, which approaches an asymptote at higher ALD cycle numbers. This trend can be rationalized by considering how the initial

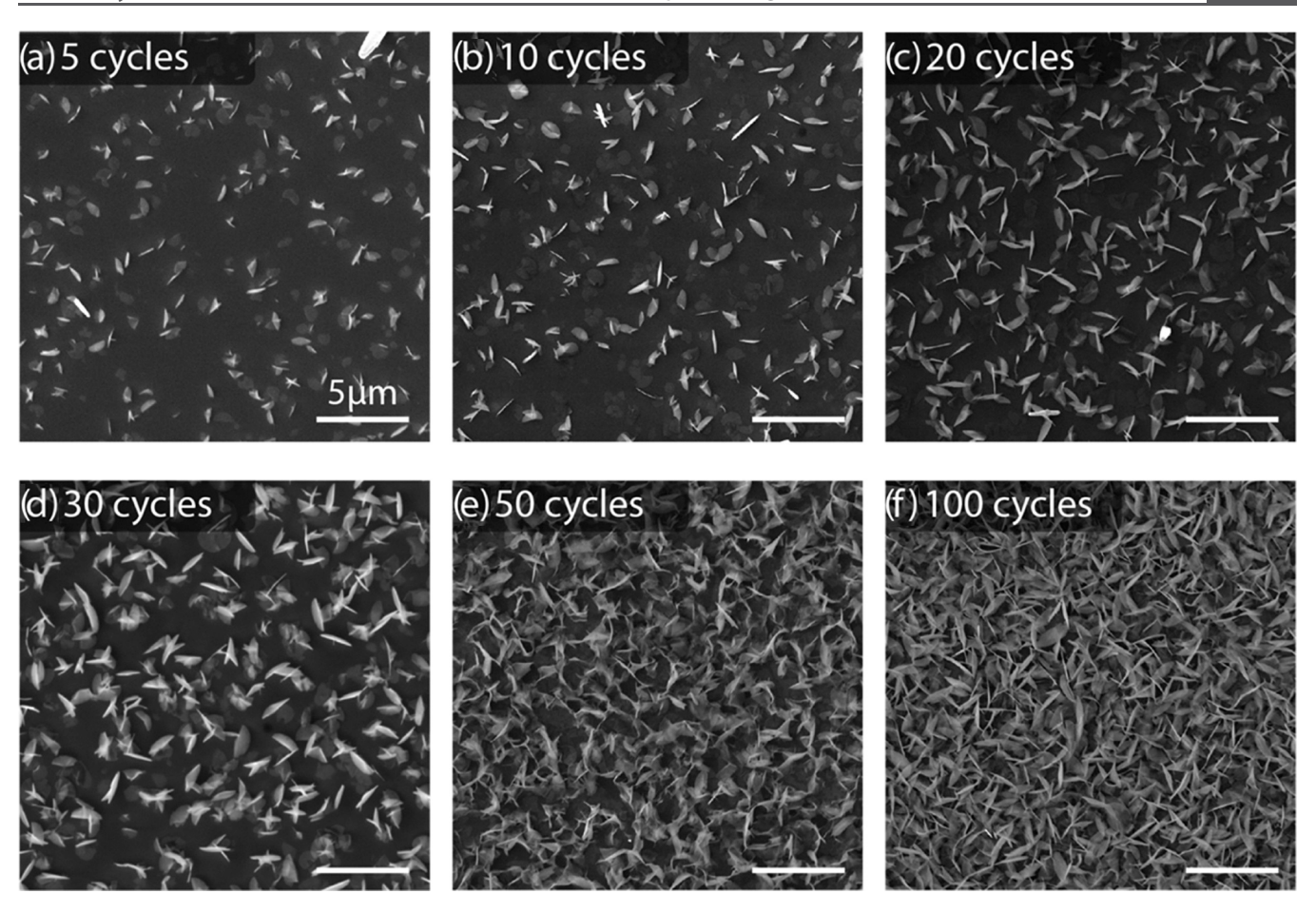


Figure 3. Zn-Al LDH nanosheet geometry as a function of the number of ALD cycles. SEM images of NSs synthesized using initial ALD Al_2O_3 films grown with (a) 5 cycles, (b) 10 cycles, (c) 20 cycles, (d) 30 cycles, (e) 50 cycles, and (f) 100 cycles.

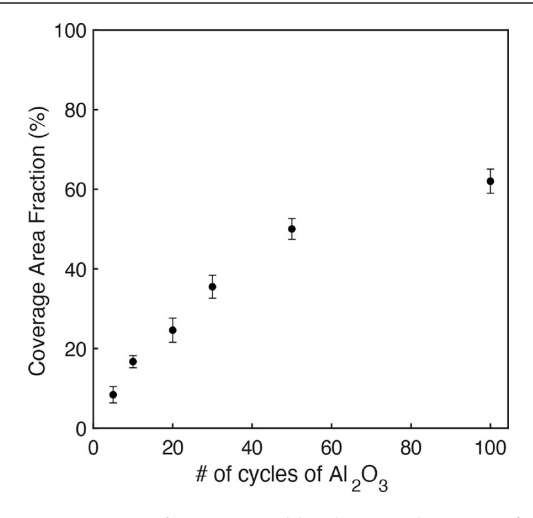


Figure 4. Percentage of area covered by the nanosheets as a function of the number (#) of cycles of Al_2O_3 . Error bars are based on 3 independent measurements at different locations within each sample.

ALD film affects the nucleation density along the surface. When the ALD film is very thin (<30 cycles), the areal nucleation density can be viewed as reactant-limited, where the spacing between nuclei is limited by the amount of Al_2O_3 available to react and form the ternary LDH phase. Therefore, the spacing between the NSs monotonically decreases as the ALD film thickness increases.

When the areal nucleation density becomes sufficiently high (after 50 cycles of ALD), the packing density of the sheets increases. This generates a steric-hindrance effect, where only the sheets that are vertically oriented (growing in the direction normal to the substrate) are able to grow, and NSs that nucleate with orientations at more acute angles relative to the substrate normal experience termination in their growth as they are blocked by adjacent sheets. As a consequence, the areal coverage fraction starts to asymptote as the spacing between nuclei that are able to successfully grow in the vertical direction reaches saturation.

To further elaborate on these nucleation mechanisms, elemental mapping was performed before and after the hydrothermal synthesis process to observe the dynamic evolution of the Al atom distribution during the nucleation and growth stages. Figure 5 shows top-down (plane-view) elemental maps of aluminum using SEM energy-dispersive Xray spectroscopy (EDS) analysis at the beginning and end of the conversion reaction. As expected, the initial ALD-deposited Al₂O₃ before conversion exhibits a uniform distribution of Al across the surface (Figure 5b,d). After 30 min of hydrothermal synthesis, we observe an accumulation of Al in discrete regions corresponding to areas of nanosheet nucleation and growth (Figure 5c,e). In the adjacent regions, a depletion of Al is observed in areas devoid of nanosheets. This accumulationdepletion behavior suggests that the mechanism for nanosheet formation is governed by the diffusion of Al along the surface, which results in a flux of Al atoms from the ALD seed layer

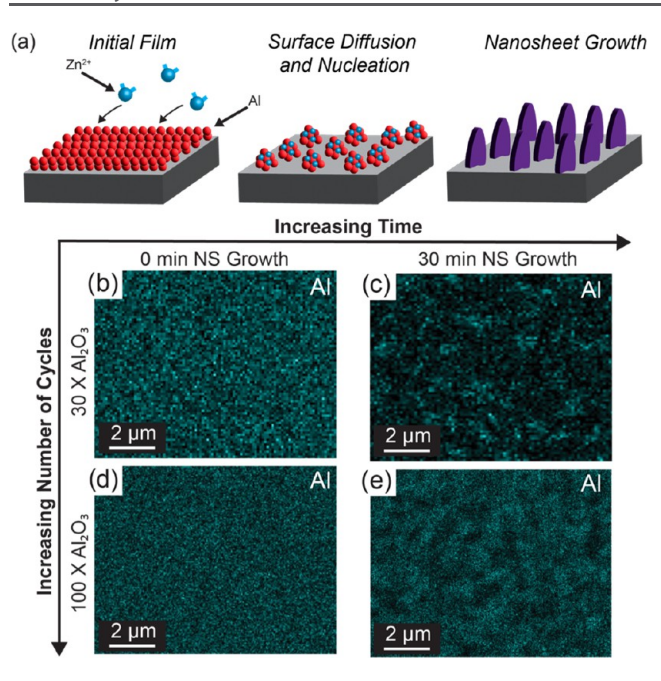


Figure 5. Accumulation/depletion of aluminum in areas corresponding to the presence and absence of nanosheets. (a) Scheme depicting the surface diffusion of Al atoms and reaction with Zn ions during the nucleation phase of nanosheet formation. Elemental mapping for different cycles of Al_2O_3 and growth times: 30 cycles of Al_2O_3 after (b) 0 min and (c) 30 min; 100 cycles of Al_2O_3 after (d) 0 min and (e) 30 min growth time.

into the nanosheets (Figure 5a). The observation of Al accumulation and depletion along the surface supports the hypothesis that Al serves as a limiting reagent in the kinetic process of the nucleation and growth of the nanosheets.

From the lens of classical nucleation theory, we can rationalize why the thickness of ALD-deposited material should correlate with the internanosheet spacing. For heterogeneous nucleation to occur, the nuclei must reach a critical radius r^* to overcome the nucleation activation barrier ΔG^* . The number of nuclei that overcome this barrier will

define the areal nucleation density, determining the number of nanosheets within a given area. The areal nucleation density is in turn determined by the flux of Al atoms along the surface, where the driving force for the diffusive flux is the concentration gradient along the surface. The nucleation sites for NSs act as aluminum "sinks" as the LDH phase forms, and the extent of the resulting concentration gradients is determined by the molar quantity of Al present in the initial film (the source of Al) or, equivalently, the ALD film thickness.

From this standpoint, we expect that as the ALD film increases in thickness, the diffusive flux of Al into the nanosheets from the adjacent regions will remain higher for a longer period of time. This would result in a higher areal nucleation density and lower internanosheet spacing, a behavior that is consistent with both Figure 4 and Figure 5. This highlights the power of ALD as an atomically precise method of controlling the film thickness with subnanometer resolution and without significant gradients in film thickness over large areas. This precise control is further illustrated by the relatively small error bars in Figure 4, which enables reliable and predictable tuning of the geometric parameters of the NS arrays. Because of these relationships between the ALD thickness and areal nucleation density, the ALD film is also expected to have an impact on the growth stage, where a continual flux of Al atoms into the nanosheets is required to facilitate the formation of the LDH phase. In particular, as suggested by the asymptotic behavior shown in Figure 4, as the inter-NS spacing saturates with thicker ALD films, one could hypothesize that nanosheet growth in the vertical direction (normal to the substrate) may become preferred. Therefore, in the following section, we examine the relationship between the ALD film thickness and nanosheet length.

Nanosheets Length Regimes. Figure 6a-f shows cross-sectional SEM images of NSs grown with different numbers of ALD cycles (5x-100x), while keeping the hydrothermal synthesis conditions constant. The average and standard deviation in NS length are plotted in Figure 6g. We observed a nonlinear trend in the length as a function of ALD film thickness, where the behavior can be characterized within three

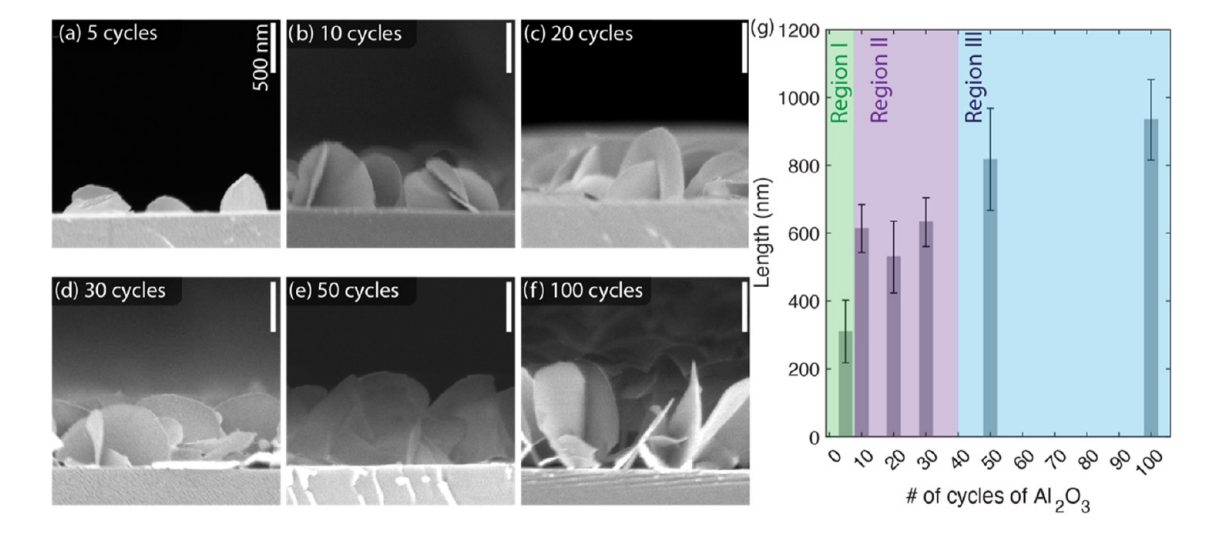


Figure 6. Zn–Al LDH nanosheet length as a function of the number of cycles of ALD. SEM images of nanosheets synthesized using initial Al_2O_3 films grown with (a) 5 cycles, (b) 10 cycles, (c) 20 cycles, (d) 30 cycles, (e) 50 cycles, and (f) 100 cycles. (g) Nanosheet length as a function of number of cycles of Al_2O_3 , categorized by three regions: (I) depletion limited, (II) length independent, and (III) steric-hindrance limited. Error bars are based on 4 independent measurements at different locations within each sample.

regions: (I) depletion limited, (II) length independent, and (III) steric-hindrance limited.

Within the first region (5x), the length of the nanosheets is depletion limited, meaning that the Al atoms from the ALD film are quickly consumed, and the hydrothermal growth is terminated at a short NS length. In the second region (10x-30x), the NS length is approximately constant (within the statistical uncertainty) as the number of ALD cycles increases. This can be rationalized by examining the trend in areal nucleation coverage shown in Figure 4, where the areal coverage fraction increases approximately linearly with increasing number of ALD cycles in the range of 10-30 cycles. This increase in surface coverage is associated with a decrease in inter-NS spacing, as discussed in the Tunable Control of Nanosheet Spacing section. Therefore, because the total mass of Al atoms is conserved and determined by the thickness of the original ALD film, as the coverage area increases approximately linearly, it follows that the length of NS will remain approximately constant. These observations illustrate the coupling between the nucleation and growth behaviors during this conversion reaction process, both of which are dictated by ALD cycle number.

In the third region (50–100x), the NS length is observed to increase once again with increasing cycles. This also can be explained by examining Figure 4, where the rate of increase (slope) in the coverage area fraction decreases for cycles 50–100. This is because of a steric-hindrance effect, where the spacing between NSs starts to approach an asymptote as the areal nucleation density increases. In other words, because the NSs cannot continue to nucleate closer together, the excess Al atoms from the original ALD films result in more vertical growth. These effects inhibit the growth at nonperpendicular angles and prevent the collapse of the nanosheet array.

Growth of Hierarchical Nanoarchitectures. To demonstrate the versatility of this process for the rational design of nanoarchitected materials on nonplanar surfaces, nanosheets were synthesized on top of various 3-D substrates including silicon microposts (Figure 7a,b), a fibrous membrane (filter paper, size 2.5 μ m) (Figure 7c) and a porous ceramic (quartz frit, Figure 7d). These substrates were chosen to highlight the versatility of the surface-directed assembly process on both flexible and nonflexible substrates, as well as geometries with both convex and concave surface topologies, including reentrant textures.

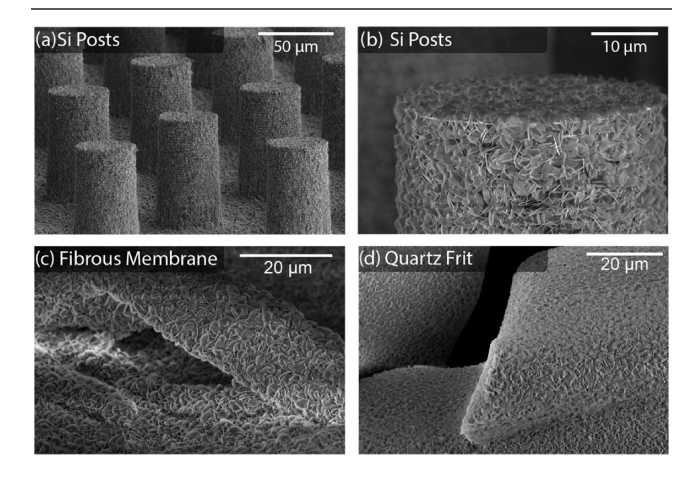


Figure 7. SEM images of hierarchical NS growth on 3-D substrates: (a, b) silicon microposts, (c) filter paper, and (d) quartz frit.

Figure 7 shows the conformality of the growth along the surface and into the pores of the 3-D templates. This conformality and uniformity in the hierarchical NS growth are facilitated by the self-limiting nature of the ALD reaction, which distributes the Al atoms uniformly throughout the porous morphology of the 3-D substrates. The ability to maintain this degree of precision in the nanoarchitecture while conformally growing material off of a complex, tortuous substrate would be challenging to accomplish with traditional solution or vapor phase growth methods. This demonstrates the power of surface-directed assembly to enable rational design of 3D nanoarchitectures without the need for any lithography or patterning steps.

To study the potential application space of the synthesized NS arrays, their stability was examined under elevated temperatures and humidity levels and across solution pH values (Figure S4). The nanosheets were able to withstand high-temperature and high-humidity environments for up to 24 h without any observable changes. Furthermore, the NS arrays remained stable under neutral and alkaline environments. However, a change in morphology was observed when the NS array was exposed to an acidic environment (pH = 4). This indicates that the NS arrays may be used as a template and/or active material for a variety of potential applications in the future and can withstand a range of relatively harsh conditions.

CONCLUSIONS

This study examines the conversion chemistry of an ALD seed layer to synthesize nanoarchitected LDH nanosheets with tunable geometries under hydrothermal growth conditions. The key findings of this study are summarized below:

- (1) Zn–Al LDH nanosheets were synthesized using a surface-directed assembly process, where ALD is used to deposit an initial Al₂O₃ seed layer that is subsequently consumed and converted to an LDH through a hydrothermal synthesis. The presence of the LDH phase and composition was confirmed with XRD and XPS
- (2) The inter-NS spacing can be tuned by changing the number of cycles of the initial Al₂O₃ film. When the film thickness is sufficiently small, the areal surface coverage of the NS arrays increases in an approximately linear manner with respect to ALD cycle number. However, as the thickness of the ALD film continues to increase, this trend approaches an asymptote. This is attributed to a steric-hindrance effect, which forces the nanosheets to grow vertically instead of continuing to increase the nucleation density.
- (3) Surface elemental mapping confirmed that aluminum acts as the limiting reagent during the nucleation stage of the hydrothermal synthesis, where Al atoms diffuse along the surface, agglomerate, and cluster into the nucleation sites where nanosheets grow.
- (4) The length of the nanosheets exhibits a nonlinear trend with respect to ALD film thickness. This growth behavior was characterized within three regions: (I) depletion limited, (II) length independent, and (III) steric hindrance. Within the first region, the Al₂O₃ film is quickly consumed, resulting in a short NS length. In the second region, the NS length is approximately constant with respect to ALD cycle number, which is attributed to

the approximately linear increase in areal nucleation density within this thickness regime. In the third region, the NS length increases once again, which is attributed to the fact that the nucleation density reaches an asymptote. Since the areal nucleation density cannot continue to increase within this steric-hindrance regime, the excess Al atoms from the original ALD films result in more vertical growth.

(5) To illustrate the versatility of this process for the rational design of 3-D nanoarchitectures, Zn—Al LDH nanosheets were conformably grown on flexible and non-flexible complex 3D substrates including silicon microposts, a porous membrane, and a quartz frit. A uniform growth of the NS array along the porous and tortuous substrate geometries was observed, including both convex and concave surface topologies.

In this study, Zn-Al LDH nanosheets were used as the model system. We aim to motivate future studies in which a variety of LDH compositions can be formed. For example, Zn²⁺ could potentially be replaced by Mg²⁺, Co²⁺, or Ni²⁺ based on previously reported hydrothermal synthesis processes. 64-66 Furthermore, we envision that the surface-directed assembly process introduced in this study will inspire a range of new conversion reactions for ALD films, with the goal of tuning 3-D geometric properties (feature size, shape, and geometry) in the resulting nanomaterial arrays. The ability to tune these geometric properties without the need for any prepatterning or lithography steps represents an important tool for materials engineers to rationally design and manufacture hierarchical nanomaterial systems, which may be composed of heterogeneous compositions of multiple different material phases and compositions. The ability to "think like an architect" and fabricate 3D nanostructures with tunable geometric parameters using this type of low-cost and scalable process could further accelerate the use of nanomaterials in applications ranging from biomedical devices to energy conversion and sustainability.

EXPERIMENTAL METHODS

Solution Fabrication. The hydrothermal growth solution was synthesized following the procedure described previously for the growth of ZnO nanowires. The following chemicals were purchased from Sigma-Aldrich: zinc nitrate hexahydrate (molecular weight: 297.49 g/mol), hexamethylenetetramine or HMTA (molecular weight: 140.19 g/mol), and polyethylenimine, branched or PEI (molecular weight: ~25 000 g/mol). 25 mM Zinc nitrate hexahydrate (25 mM) was mixed with 25 mM HMTA, 5 mM PEI, and 1000 mL of deionized water (DI water). To dissolve the chemicals, the solution was stirred (250 rpm) at 95 °C for 30 min. It was allowed to cool in a water bath. After the solution reached a temperature of ~60 °C, it was filtered three times (with 8, 2.5, and 0.22 μ m filters) using a vacuum filtration assembly (Sigma-Aldrich).

Seed Layer Deposition. The Al_2O_3 seed layers were deposited using a lab-built and hot-walled crossflow atomic layer deposition reactor. 5, 10, 20, 30, 50, and 100 cycles of Al_2O_3 were deposited using trimethylaluminum (TMA) and DI water as the chemical precursors at a temperature of 150 °C and a ~ 1.6 Å/cycle growth rate. Before the ALD deposition, the silicon wafers and silicon micropost substrates were cleaned with oxygen plasma for 20 min using a plasma cleaner (Harrick Plasma). Filter paper substrates were baked at 105 °C using a convection oven (Thermo Scientific) for 24 h prior to the ALD deposition. Quartz frit substrates were sonicated in 1 M HCl for 3 min and were subsequently baked in the convection oven for an hour.

Hydrothermal Synthesis. The hydrothermal growth process was performed using the procedure described previously. The growth of nanosheets and the formation of the LDH phase in this study result from the use of Al_2O_3 , rather than ZnO as the seed layer, while the hydrothermal growth solution composition and synthesis procedure remained the same. Nanosheets were synthesized at a temperature of 87 °C while stirring at 350 rpm for 30 min. Before hydrothermal synthesis, the substrates were cleaned with oxygen plasma for 5 min using a plasma cleaner (Harrick Plasma).

Conversion Reaction. The conversion reaction from Al₂O₃ to the Zn-Al LDH phase has been previously reported to follow two possible mechanisms, depending on the solution pH. At near-neutral pH values, Al₂O₃ may solvate to undergo surface hydrolysis, thereby creating a hydrolyzed layer that reacts with Zn2+ ions in solution to form Zn-Al LDH. 52,53 A second possible mechanism suggests that presence of the additive HMTA may create a locally alkaline environment near the reaction surface by thermally decomposing during the hydrothermal synthesis reaction. 34,54,55 In the reaction conditions used in this study, while the solution chemistry is initially neutral, the increase in pH associated with HMTA decomposition could also allow for the formation of reaction intermediates such as Al(OH)₄⁻ and Zn(OH), which can subsequently react to form the Zn-Al LDH phase at the substrate surface. It is possible that either, or both, of these reactions may contribute to the observed conversion processes in this study.

Materials Characterization. Top-view SEM images of the nanosheets were taken using a TESCAN RISE SEM with a voltage of 5.0 kV and a beam intensity of 10. For the quartz frit, the beam intensity was lowered to 3. Cross-sectional imaging of the nanosheets was performed using a TFS Helios 650 Nanolab SEM/FIB microscope with a voltage of 2.0 kV and a current of 100 pA. To reduce charging during SEM imaging of the NS samples, gold was sputtered on top of the substrates for 10 s using an SPI-Module Carbon/Sputter Coater. The SEM-EDS elemental maps shown in Figure 5 were taken using a TESCAN MIRA3 SEM.

For cross-sectional STEM imaging and EDS, nanosheets were sectioned using a plasma focused-ion beam (PFIB) and transferred onto a TEM grid using a Thermo Fisher Helios G4 PFIB UXe. Using a Thermo Fisher Talos F200X G2 S/TEM, a single nanosheet was isolated and imaged using a HAADF detector, and elemental mapping was performed by EDS. In addition to elemental maps, a line scan was collected when viewing the nanosheet along the edge.

Grazing incidence XRD was performed using a Rigaku SmartLab X-ray diffractometer with an incidence angle of 0.5°. XPS measurements were taken using a Kratos Axis Ultra X-ray photoelectron spectrometer with a spot size of $700 \times 300~\mu\text{m}^2$. A monochromatic Al source (10 mA, 12 kV) and pass energies of 160 eV (for the survey scans) and 20 eV (for the core scans) were used during scanning.

Quantitative Image Analysis. The covered area of the nanosheets was measured for the top-view SEM images (with field of view between 5 and 10 μ m, for accuracy) using ImageJ. First, the image was converted to an 8-bit gray image. The area coverage fraction was obtained by thresholding the image. The area covered by the nanosheets was measured at three different positions within the same sample.

The length of the nanosheets was manually measured from the cross-sectional SEM images using ImageJ. The length of the nanosheets was calculated from top to bottom, disregarding the orientation angle. The length of 20 nanosheets was averaged by measuring 5 different nanosheets at 4 different positions.

ASSOCIATED CONTENT

Supporting Information

The Supporting Information is available free of charge at https://pubs.acs.org/doi/10.1021/acs.chemmater.4c01194.

SEM image of ZnO homogeneous precipitates formed during hydrothermal synthesis (Figure S1); XRD pattern of LDH nanosheets with increasing hydro-

thermal growth time (Figure S2); thin-film thickness as a function of ALD cycle number for Al_2O_3 (Figure S3); and stability tests for LDH nanosheets at high humidity, chemical exposure, and high temperature (Figure S4) (PDF)

AUTHOR INFORMATION

Corresponding Author

Neil P. Dasgupta — Department of Mechanical Engineering, University of Michigan, Ann Arbor, Michigan 48109, United States; Department of Materials Science and Engineering, University of Michigan, Ann Arbor, Michigan 48109, United States; orcid.org/0000-0002-5180-4063; Email: ndasgupt@umich.edu

Authors

Alondra M. Ortiz-Ortiz — Department of Mechanical Engineering, University of Michigan, Ann Arbor, Michigan 48109, United States; orcid.org/0009-0004-4312-4449

Daniel O. Delgado Cornejo — Department of Materials Science and Engineering, University of Michigan, Ann Arbor, Michigan 48109, United States; orcid.org/0009-0002-3484-5960

Kalyn M. Fuelling – Department of Materials Science and Engineering, University of Michigan, Ann Arbor, Michigan 48109, United States; orcid.org/0009-0004-1038-4746

Ashley R. Bielinski — Department of Mechanical Engineering, University of Michigan, Ann Arbor, Michigan 48109, United States; Materials Science Division, Argonne National Laboratory, Lemont, Illinois 60439, United States

Tao Ma – Michigan Center for Materials Characterization, University of Michigan, Ann Arbor, Michigan 48109, United States; Orcid.org/0000-0002-0579-8045

Complete contact information is available at: https://pubs.acs.org/10.1021/acs.chemmater.4c01194

Author Contributions

¹A.M.O.-O. and D.O.D.C. contributed equally.

Notes

The authors declare no competing financial interest.

ACKNOWLEDGMENTS

This work was supported by the National Science Foundation under grant nos. 1751590 and 2131709. A.M.O.-O. acknowledges support from the National Science Foundation Graduate Research Fellowship Program under grant no. DGE-1256260. Argonne National Laboratory's contribution is based upon work supported by Laboratory Directed Research and Development (LDRD) funding from Argonne National Laboratory, provided by the Director, Office of Science, of the U.S. Department of Energy under Contract No. DE-AC02-06CH11357. The authors thank Dr. Anish Tuteja for the guidance and support throughout this study. The authors thank Tae H. Cho and Daniel W. Liao for assistance with XPS analysis and Kelsey Ramp for valuable discussions on the reaction mechanisms. The authors acknowledge the University of Michigan College of Engineering and NSF #DMR-1625671 for financial support and the Michigan Center for Materials Characterization for use of the instruments and staff assistance. The authors thank Allen H. Hunter and Haiping Sun for their guidance and support during the process of characterizing the nanosheets using TEM and XPS.

REFERENCES

- (1) Xu, C.; Anusuyadevi, P. R.; Aymonier, C.; Luque, R.; Marre, S. Nanostructured Materials for Photocatalysis. *Chem. Soc. Rev.* **2019**, 48 (14), 3868–3902.
- (2) Naresh, V.; Lee, N. A Review on Biosensors and Recent Development of Nanostructured Materials-Enabled Biosensors. *Sensors* **2021**, *21*, 1109.
- (3) Bhati, V. S.; Hojamberdiev, M.; Kumar, M. Enhanced Sensing Performance of ZnO Nanostructures-Based Gas Sensors: A Review. *Energy Rep.* **2020**, *6*, 46–62.
- (4) Li, Z.; Fan, Q.; Yin, Y. Colloidal Self-Assembly Approaches to Smart Nanostructured Materials. *Chem. Rev.* **2022**, *122* (5), 4976–5067.
- (5) Zhou, G.; Xu, L.; Hu, G.; Mai, L.; Cui, Y. Nanowires for Electrochemical Energy Storage. *Chem. Rev.* **2019**, *119* (20), 11042–11109.
- (6) Wang, Y.; Cao, G. Developments in Nanostructured Cathode Materials for High-Performance Lithium-Ion Batteries. *Adv. Mater.* **2008**, 20 (12), 2251–2269.
- (7) Ji, L.; Lin, Z.; Alcoutlabi, M.; Zhang, X. Recent Developments in Nanostructured Anode Materials for Rechargeable Lithium-Ion Batteries. *Energy Environ. Sci.* **2011**, *4* (8), 2682–2699.
- (8) Dasgupta, N. P.; Sun, J.; Liu, C.; Brittman, S.; Andrews, S. C.; Lim, J.; Gao, H.; Yan, R.; Yang, P. 25th Anniversary Article: Semiconductor Nanowires Synthesis, Characterization, and Applications. *Adv. Mater.* **2014**, *26*, 2137.
- (9) Burchak, O.; Keller, C.; Lapertot, G.; Salaün, M.; Danet, J.; Chen, Y.; Bendiab, N.; Pépin-Donat, B.; Lombard, C.; Faure-Vincent, J.; et al. Scalable Chemical Synthesis of Doped Silicon Nanowires for Energy Applications. *Nanoscale* 2019, 11 (46), 22504–22514.
- (10) Shu, Z.; Jiao, X.; Chen, D. Synthesis and Photocatalytic Properties of Flower-like Zirconia Nanostructures. *CrystEngComm* **2012**, *14* (3), 1122–1127.
- (11) Yang, X.; Li, J.; Liang, T.; Ma, C.; Zhang, Y.; Chen, H.; Hanagata, N.; Su, H.; Xu, M. Antibacterial Activity of Two-Dimensional MoS2 Sheets. *Nanoscale* **2014**, *6* (17), 10126–10133.
- (12) Greer, J. R.; Deshpande, V. S. Three-Dimensional Architected Materials and Structures: Design, Fabrication, and Mechanical Behavior. *MRS Bull.* **2019**, 44 (10), 750–757.
- (13) Vyatskikh, A.; Delalande, S.; Kudo, A.; Zhang, X.; Portela, C. M.; Greer, J. R. Additive Manufacturing of 3D Nano-Architected Metals. *Nat. Commun.* **2018**, 9 (1), No. 593.
- (14) Liang, Y.; Sias, D.; Chen, P. J.; Tawfick, S. Tough Nano-Architectured Conductive Textile Made by Capillary Splicing of Carbon Nanotubes. *Adv. Eng. Mater.* **2017**, *19* (7), No. 1600845.
- (15) Huang, Y.; Duan, X.; Wei, Q.; Lieber, C. M. Directed Assembly of One-Dimensional Nanostructures into Functional Networks. *Science* **2001**, 291 (5504), 630–633.
- (16) Yang, P.; Yan, H.; Mao, S.; Russo, R.; Johnson, J.; Saykally, R.; Morris, N.; Pham, J.; He, R.; Choi, H.-J. Controlled Growth of ZnO Nanowires and Their Optical Properties. *Adv. Funct. Mater.* **2002**, *12* (5), 323–331.
- (17) Kim, Y.; Drews, A.; Chandrasekaran, R.; Miller, T.; Sakamoto, J. Improving Li-Ion Battery Charge Rate Acceptance through Highly Ordered Hierarchical Electrode Design. *Ionics* **2018**, *24* (10), 2935–2943.
- (18) Xiang, C.; Meng, A. C.; Lewis, N. S. Evaluation and Optimization of Mass Transport of Redox Species in Silicon Microwire-Array Photoelectrodes. *Proc. Natl. Acad. Sci. U.S.A.* **2012**, 109 (39), 15622–15627.
- (19) Bielinski, A. R.; Gayle, A. J.; Lee, S.; Dasgupta, N. P. Geometric Optimization of Bismuth Vanadate Core–Shell Nanowire Photoanodes Using Atomic Layer Deposition. *ACS Appl. Mater. Interfaces* **2021**, *13* (44), 52063–52072.
- (20) Wang, J.; Lee, S.; Bielinski, A. R.; Meyer, K. A.; Dhyani, A.; Ortiz-Ortiz, A. M.; Tuteja, A.; Dasgupta, N. P. Rational Design of Transparent Nanowire Architectures with Tunable Geometries for Preventing Marine Fouling. *Adv. Mater. Interfaces* **2020**, *7*, No. 2000672, DOI: 10.1002/admi.202000672.

- (21) Biswas, A.; Bayer, I. S.; Biris, A. S.; Wang, T.; Dervishi, E.; Faupel, F. Advances in Top-down and Bottom-up Surface Nanofabrication: Techniques, Applications & Future Prospects. *Adv. Colloid Interface Sci.* **2012**, *170*, 2.
- (22) Tseng, A. A. Nanofabrication: Fundamentals and Applications; World Scientific, 2008.
- (23) Arole, V. M.; Munde, S. V. Fabrication of Nanomaterials by Top-down and Bottom-up Approaches-an Overview. *J. Mater. Sci.* **2014**, *1*, 89–93.
- (24) Yu, H.-D.; Regulacio, M. D.; Ye, E.; Han, M.-Y. Chemical Routes to Top-down Nanofabrication. *Chem. Soc. Rev.* **2013**, 42 (14), 6006–6018.
- (25) Xia, D.; Ku, Z.; Lee, S. C.; Brueck, S. R. J. Nanostructures and Functional Materials Fabricated by Interferometric Lithography. *Adv. Mater.* **2011**, 23 (2), 147–179.
- (26) Xie, Q.; Hong, M. H.; Tan, H. L.; Chen, G. X.; Shi, L. P.; Chong, T. C. Fabrication of Nanostructures with Laser Interference Lithography. J. Alloys Compd. 2008, 449 (1–2), 261–264.
- (27) Li, P.; Chen, S.; Dai, H.; Yang, Z.; Chen, Z.; Wang, Y.; Chen, Y.; Peng, W.; Shan, W.; Duan, H. Recent Advances in Focused Ion Beam Nanofabrication for Nanostructures and Devices: Fundamentals and Applications. *Nanoscale* **2021**, *13* (3), 1529–1565.
- (28) Zhang, W.; Li, Z.; Dang, R.; Tran, T. T.; Gallivan, R. A.; Gao, H.; Greer, J. R. Suppressed Size Effect in Nanopillars with Hierarchical Microstructures Enabled by Nanoscale Additive Manufacturing. *Nano Lett.* **2023**, 23 (17), 8162–8170.
- (29) Rorem, B. A.; Cho, T. H.; Farjam, N.; Lenef, J. D.; Barton, K.; Dasgupta, N. P.; Guo, L. J. Integrating Structural Colors with Additive Manufacturing Using Atomic Layer Deposition. *ACS Appl. Mater. Interfaces* **2022**, *14* (27), 31099–31108.
- (30) Cho, T. H.; Farjam, N.; Allemang, C. R.; Pannier, C. P.; Kazyak, E.; Huber, C.; Rose, M.; Trejo, O.; Peterson, R. L.; Barton, K.; Dasgupta, N. P. Area-Selective Atomic Layer Deposition Patterned by Electrohydrodynamic Jet Printing for Additive Manufacturing of Functional Materials and Devices. *ACS Nano* 2020, 14 (12), 17262–17272.
- (31) Fourkas, J. T.; Gao, J.; Han, Z.; Liu, H.; Marmiroli, B.; Naughton, M. J.; Petersen, J. S.; Sun, Y.; Vagilio Pret, A.; Zheng, Y. Grand Challenges in Nanofabrication: There Remains Plenty of Room at the Bottom. *Front. Nanotechnol.* **2021**, *3*, No. 700849, DOI: 10.3389/fnano.2021.700849.
- (32) Bielinski, A. R.; Kazyak, E.; Schlepütz, C. M.; Jung, H. J.; Wood, K. N.; Dasgupta, N. P. Hierarchical ZnO Nanowire Growth with Tunable Orientations on Versatile Substrates Using Atomic Layer Deposition Seeding. *Chem. Mater.* **2015**, *27*, 4799.
- (33) Conley, J. F.; Stecker, L.; Ono, Y. Directed Assembly of ZnO Nanowires on a Si Substrate without a Metal Catalyst Using a Patterned ZnO Seed Layer. *Nanotechnology* **2005**, *16* (2), 292.
- (34) Greene, L. E.; Yuhas, B. D.; Law, M.; Zitoun, D.; Yang, P. Solution-Grown Zinc Oxide Nanowires. *Inorg. Chem.* **2006**, *45*, 7535.
- (35) Barton, H. F.; Davis, A. K.; Parsons, G. N. The Effect of Surface Hydroxylation on MOF Formation on ALD Metal Oxides: MOF-525 on TiO2/Polypropylene for Catalytic Hydrolysis of Chemical Warfare Agent Simulants. ACS Appl. Mater. Interfaces 2020, 12 (13), 14690–14701.
- (36) Bielinski, A. R.; Boban, M.; He, Y.; Kazyak, E.; Lee, D. H.; Wang, C.; Tuteja, A.; Dasgupta, N. P. Rational Design of Hyperbranched Nanowire Systems for Tunable Superomniphobic Surfaces Enabled by Atomic Layer Deposition. *ACS Nano* **2017**, *11*, 478.
- (37) George, S. M. Atomic Layer Deposition: An Overview. Chem. Rev. 2010, 110, 111.
- (38) Gayle, A. J.; Berquist, Z. J.; Chen, Y.; Hill, A. J.; Hoffman, J. Y.; Bielinski, A. R.; Lenert, A.; Dasgupta, N. P. Tunable Atomic Layer Deposition into Ultra-High-Aspect-Ratio (>60000:1) Aerogel Monoliths Enabled by Transport Modeling. *Chem. Mater.* **2021**, 33 (14), 5572–5583.
- (39) Ortiz-Ortiz, A. M.; Gayle, A. J.; Wang, J.; Faustyn, H. R.; Penley, D.; Sherwood, C.; Tuteja, A.; Dasgupta, N. P. Scaling-Up

- Seeded Hydrothermal Nanowire Synthesis on Non-Planar Surfaces Using a Flow Reactor. ACS Appl. Eng. Mater. 2023, 1 (6), 1583–1592
- (40) Lenef, J. D.; Gayle, A. J.; Jo, J.; Fuelling, K. M.; Yadavalli, S. K.; Ortiz-Ortiz, A. M.; Sun, K.; Peterson, R. L.; Dasgupta, N. P. Tunable Sulfur Incorporation into Atomic Layer Deposition Films Using Solution Anion Exchange. *Chem. Mater.* **2023**, *35* (6), 2503–2517.
- (41) Seenivasan, S.; Jung, H.; Han, J. W.; Kim, D.-H. Surface Roughening Strategy for Highly Efficient Bifunctional Electrocatalyst: Combination of Atomic Layer Deposition and Anion Exchange Reaction. *Small Methods* **2022**, *6* (2), No. 2101308.
- (42) Isakov, K.; Kauppinen, C.; Franssila, S.; Lipsanen, H. Superhydrophobic Antireflection Coating on Glass Using Grass-like Alumina and Fluoropolymer. ACS Appl. Mater. Interfaces 2020, 12 (44), 49957–49962.
- (43) Kauppinen, C.; Isakov, K.; Sopanen, M. Grass-like Alumina with Low Refractive Index for Scalable, Broadband, Omnidirectional Antireflection Coatings on Glass Using Atomic Layer Deposition. ACS Appl. Mater. Interfaces 2017, 9 (17), 15038–15043.
- (44) Li, X.; Yu, L.; Wang, G.; Wan, G.; Peng, X.; Wang, K.; Wang, G. Hierarchical NiAl LDH Nanotubes Constructed via Atomic Layer Deposition Assisted Method for High Performance Supercapacitors. *Electrochim. Acta* 2017, 255, 15–22.
- (45) Xia, X.; Zhang, Y.; Chao, D.; Xiong, Q.; Fan, Z.; Tong, X.; Tu, J.; Zhang, H.; Fan, H. J. Tubular TiC Fibre Nanostructures as Supercapacitor Electrode Materials with Stable Cycling Life and Wide-Temperature Performance. *Energy Environ. Sci.* **2015**, 8 (5), 1559–1568.
- (46) Khaletskaya, K.; Turner, S.; Tu, M.; Wannapaiboon, S.; Schneemann, A.; Meyer, R.; Ludwig, A.; Van Tendeloo, G.; Fischer, R. A. Self-Directed Localization of ZIF-8 Thin Film Formation by Conversion of ZnO Nanolayers. *Adv. Funct. Mater.* **2014**, *24* (30), 4804–4811.
- (47) Weiß, A.; Goldmann, J.; Kettunen, S.; Popov, G.; Iivonen, T.; Mattinen, M.; Jalkanen, P.; Hatanpää, T.; Leskelä, M.; Ritala, M.; Kemell, M. Conversion of ALD CuO Thin Films into Transparent Conductive P-Type CuI Thin Films. *Adv. Mater. Interfaces* **2023**, *10* (3), No. 2201860.
- (48) Mäntymäki, M.; Mizohata, K.; Heikkilä, M. J.; Räisänen, J.; Ritala, M.; Leskelä, M. Studies on Li3AlF6 Thin Film Deposition Utilizing Conversion Reactions of Thin Films. *Thin Solid Films* **2017**, 636, 26–33
- (49) Thimsen, E.; Peng, Q.; Martinson, A. B. F.; Pellin, M. J.; Elam, J. W. Ion Exchange in Ultrathin Films of Cu2S and ZnS under Atomic Layer Deposition Conditions. *Chem. Mater.* **2011**, 23 (20), 4411–4413
- (50) Zhou, Z.; Xu, L.; Ding, Y.; Xiao, H.; Shi, Q.; Li, X.; Li, A.; Fang, G. Atomic Layer Deposition Meets Metal—Organic Frameworks. *Prog. Mater. Sci.* **2023**, *138*, No. 101159.
- (51) Kim, Y.; Woo, W. J.; Kim, D.; Lee, S.; Chung, S.; Park, J.; Kim, H. Atomic-Layer-Deposition-Based 2D Transition Metal Chalcogenides: Synthesis, Modulation, and Applications. *Adv. Mater.* **2021**, 33 (47), No. 2005907.
- (52) Wan, B.; Yan, Y.; Huang, R.; Abdala, D. B.; Liu, F.; Tang, Y.; Tan, W.; Feng, X. Formation of Zn-Al Layered Double Hydroxides (LDH) during the Interaction of ZnO Nanoparticles (NPs) with γ-Al₂O₃. *Sci. Total Environ.* **2019**, *650*, 1980–1987.
- (53) Li, W.; Livi, K. J. T.; Xu, W.; Siebecker, M. G.; Wang, Y.; Phillips, B. L.; Sparks, D. L. Formation of Crystalline Zn–Al Layered Double Hydroxide Precipitates on γ-Alumina: The Role of Mineral Dissolution. *Environ. Sci. Technol.* **2012**, 46 (21), 11670–11677.
- (54) Liu, Y.; Dai, C.; Wang, K.; Zhao, M.; Zhao, G.; Yang, S.; Yan, Z.; You, Q. New Insights into the Hydroquinone (HQ)-Hexamethylenetetramine (HMTA) Gel System for Water Shut-off Treatment in High Temperature Reservoirs. *J. Ind. Eng. Chem.* **2016**, 35, 20.
- (55) Strom, J. G.; Jun, H. W. Kinetics of Hydrolysis of Methenamine. J. Pharm. Sci. 1980, 69 (11), 1261–1263.

- (56) Zhao, J.; Miao, P.; Zhang, X.; Wang, P.; Li, Z.; Wu, L.-Z.; Shi, R.; Zhang, T. Photothermal Mineralization of Polyolefin Microplastics via TiO2 Hierarchical Porous Layer-Based Semiwetting Air-Plastic-Solid Interfaces. *Adv. Mater.* **2024**, *36* (25), No. 2400681.
- (57) Peng, L.; Wang, C.; Wang, Q.; Shi, R.; Zhang, T.; Waterhouse, G. I. N. Rationally Designed Ni–Ni3S2 Interfaces for Efficient Overall Water Electrolysis. *Adv. Energy Sustainable Res.* **2021**, 2 (11), No. 2100078.
- (58) Fan, K.; Li, Z.; Song, Y.; Xie, W.; Shao, M.; Wei, M. Confinement Synthesis Based on Layered Double Hydroxides: A New Strategy to Construct Single-Atom-Containing Integrated Electrodes. *Adv. Funct. Mater.* **2021**, *31* (10), No. 2008064.
- (59) Bukhtiyarova, M. V. A Review on Effect of Synthesis Conditions on the Formation of Layered Double Hydroxides. *J. Solid State Chem.* **2019**, *269*, 494.
- (60) Auerbach, S. M.; Carrado, K. A.; Dutta, P. K. Handbook of Layered Materials; M. Dekker: New York, 2004.
- (61) Radha, A. V.; Kamath, P. V.; Shivakumara, C. Order and Disorder among the Layered Double Hydroxides: Combined Rietveld and DIFFaX Approach. *Acta Crystallogr., Sect. B* **2007**, *63* (2), 243–250.
- (62) Radha, A. V.; Kamath, P. V.; Shivakumara, C. Conservation of Order, Disorder, and "Crystallinity" during Anion-Exchange Reactions among Layered Double Hydroxides (LDHs) of Zn with Al. *J. Phys. Chem. B* **2007**, *111* (13), 3411–3418.
- (63) Kothandaraman, C. P. Fundamentals of Heat and Mass Transfer, 3rd ed.; New Age International (P) Ltd., Publishers: New Delhi.
- (64) Xu, Z. P.; Lu, G. Q. Hydrothermal Synthesis of Layered Double Hydroxides (LDHs) from Mixed MgO and Al2O3: LDH Formation Mechanism. *Chem. Mater.* **2005**, *17* (5), 1055–1062.
- (65) Sun, Y.; Zhou, J.; Cai, W.; Zhao, R.; Yuan, J. Hierarchically Porous NiAl-LDH Nanoparticles as Highly Efficient Adsorbent for p-Nitrophenol from Water. *Appl. Surf. Sci.* **2015**, *349*, 897–903.
- (66) Zhao, J.; Liu, J.; Li, Z.; Wang, K.; Shi, R.; Wang, P.; Wang, Q.; Waterhouse, G. I. N.; Wen, X.; Zhang, T. Ruthenium-Cobalt Single Atom Alloy for CO Photo-Hydrogenation to Liquid Fuels at Ambient Pressures. *Nat. Commun.* **2023**, *14* (1), No. 1909.